The Complexity of Hydration of Phloroglucinol: A Comprehensive Structural and Thermodynamic Characterization

Doris E. Braun,*,[†] Derek A. Tocher,[†] Sarah L. Price,[†] and Ulrich J. Griesser[‡]

[†]Department of Chemistry, University College London, 20 Gordon Street, London WC1H 0AJ, U.K.
[‡]Institute of Pharmacy, University of Innsbruck, Innrain 52, 6020 Innsbruck, Austria

S *Supporting Information*

ABSTRACT: Hydrate formation is of great importance as the inclusion of water molecules affects many solid state properties and hence determines the required chemical processing, handling, and storage. Phloroglucinol is industrially important, and the observed differences in the morphology and diffuse scattering effects with growth conditions have been scientifically controversial. We have studied the anhydrate and dihydrate of phloroglucinol and their transformations by a unique combination of complementary experimental and computational techniques, namely, moisture sorption analysis, hot-stage microscopy, differential scanning calorimetry, thermogravimetry, isothermal calorimetry, single crystal and powder

X-ray diffractometry, and crystal energy landscape calculations. The enthalpically stable dihydrate phase is unstable below 16% relative humidity (25 °C) and above 50 °C (ambient humidity), and the kinetics of hydration/dehydration are relatively rapid with a small hysteresis. A consistent atomistic picture of the thermodynamics of the hydrate/anhydrate transition was derived, consistent with the disordered single X-ray crystal structure and crystal energy landscape showing closely related low energy hydrate structures. These structures provide models for proton disorder and show stacking faults as intergrowth of different layers are possible. This indicates that the consequent variability in crystal surface features and diffuse scattering with growth conditions is not a practical concern.
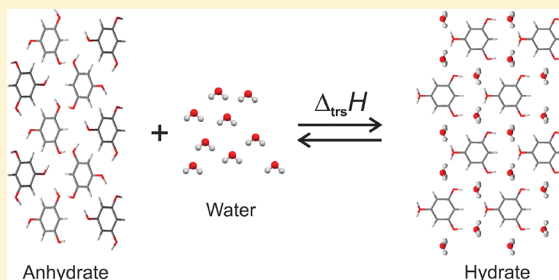
1. INTRODUCTION

The formation of solvated and in particular hydrated forms, in which solvent molecules occupy regular positions in the crystal structure, is widespread for pharmaceutical materials.[1−3] Recent statistical surveys based on the results of 245 polymorph screens of organic compounds[4] and our own evaluation of the literature on 960 organic drug compounds[5,6] present in the European Pharmacopoeia[7] revealed that ca. one-third of these compounds exist as hydrates. Furthermore, according to our statistics,[5,6] more than 40% of all compounds that are known to form hydrates are used and specified as water adducts in the Pharmacopoeia.[5,6] During the manufacturing process, the drug compound is often in contact with water (for example during crystallization, freeze-drying, wet granulation, aqueous film-coating, spray drying, storage, etc.). Consequently, knowledge of hydration and dehydration conditions is essential, as the presence of water in the crystal lattice may lead to very different physicochemical properties, such as solubility, dissolution rate, chemical stability, and bioavailability.[8−10] Thus, finding and characterizing the range of possible hydrates is fundamental to drug development; however, it is time-consuming and requires effective strategies combining a variety of techniques.[11−13]

The widely used, experimental screening approaches for solid forms, which include solvent crystallization and slurry conversions in aqueous solvents as well as dynamic moisture sorption studies, may quickly indicate the formation of

hydrate(s).[13] However, they do not provide insight into the structural and thermodynamic reasons for hydrate formation. X-ray diffraction and spectroscopic methods, combined with calorimetric (differential scanning calorimetry, solution calorimetry, etc.) and solubility measurements can generate a complete structural and thermodynamic description of a hydrate/anhydrate system. However, if it is difficult to obtain large amounts of the pure phases and representative crystals suitable for single crystal X-ray diffraction, then this picture will be incomplete. Hence the computational generation of thermodynamically feasible crystal structures offers a complementary technique, and provides a molecular level understanding of the related compounds that often cannot be achieved by experimental techniques alone. For example, crystal structure prediction (CSP) techniques have been used to rationalize the formation and structures of various stoichiometric hydrates of dihydroxybenzoic acids,[14] some diastereomeric salt pairs,[15] and racemic and enantiopure naproxen.[16]

Phloroglucinol (1,3,5-trihydroxybenzene, PhG, Figure 1) is a small, symmetrical organic molecule whose dihydrate[17] (Hy2) and anhydrous (AH) forms[18] have been widely investigated. PhG is used as a precursor for the synthesis of a variety of
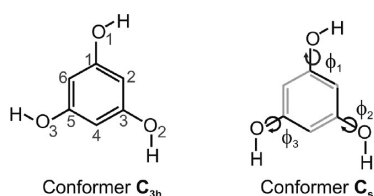
Figure 1. The two low energy conformers of the PhG molecule and the atom numbering used throughout this study. The intramolecular degrees of freedom (torsions and H−O−C angles) that were optimized in the lattice energy minimizations are indicated with arrows (ϕ_1: C2−C1−O1−H, ϕ_2: C2−C3−O2−H, and ϕ_3: C4−C5−O3−H) and emboldened on the less stable C_s conformer.

industrial products such as pharmaceuticals, dyes, and explosives.[19−21] It is the parent compound for a high number of derivatives, called phloroglucinols, which are present in a number of plants and algae.[22] The compound exhibits a broad spectrum of pharmacological activities: antibacterial, antiviral, antifungal, antioxidant, and antidepressant.[23−25] PhG itself is therapeutically used as a spasmolytic agent[26] and disinfectant.[27] Only the enol tautomer of PhG has to be considered, as it is far more stable than the keto form.[28]

There have been several X-ray crystallographic studies on PhG because it readily crystallizes in the Hy2 form, but with variable morphologies and crystal quality, with even the best quality crystals showing diffuse scattering effects. The Hy2 structure was first studied in 1917 when the lattice parameters were reported.[29] Banerjee and Ahmand,[30] Bose and Sen,[31] and Chorgade[32] independently determined the cell constants, and they proposed possible space groups and a potential crystal structure. Wallwork and Powell[17] reported the Hy2 structure (Cambridge Structural Database (CSD) Refcode:[39] PHGLOH) and proposed a model for the observed diffuse thermal reflections and disorder streaks, but they did not locate the polar protons. Subsequently, Singh and Singh[33] reinvestigated the growth and disorder of the Hy2 crystals, confirming the results observed by Wallwork and Powell.[17] Singh and Singh proposed a link between the crystal morphologies and surface features, which they found to depend on growth conditions, to the diffuse scattering effects.[33] Saha et al. (CSD Refcode: PHGLOH01) redetermined the Hy2 structure, including all proton positions.[34] Very recently, Thomas et al. also investigated Hy2 and proposed a model for the Hy2 diffuse scattering based on first-principles solid-state quantum mechanical calculations.[35] Other joint experimental and theoretical studies on PhG include investigations into the dipole moment of PhG in ethanol,[36] and vapor pressure and lattice energy calculations.[37] The interactions of each of the two PhG conformers with water molecules were modeled computationally in vacuo and in water solution.[38] The less readily obtained anhydrate structure has also been determined at room temperature by Maartmann-Moe[18] (CSD Refcode: PHGLOL) and redetermined at 105 K (CSD Refcode: PHGLOL01) by Goerbitz et al.[40]

The present study develops a consistent quantitative account of the solid state properties and the structural and thermodynamic features of the AH/Hy2 system. A broad range of analytical techniques are applied to resolve and characterize the complexity of the PhG solid forms emerging from a polymorph screen, including hot-stage microscopy (HTM), differential scanning calorimetry (DSC), thermogravimetric analysis (TGA), relative humidity (RH)-perfusion and

solution calorimetry, X-ray diffractometry (powder and single crystal), Infrared spectroscopy (IR), and dynamic moisture sorption analysis. The relative enthalpy of AH and Hy2 could only be established using innovative approaches of solution (RH-perfusion)[41] and DSC measurements,[42] as recently demonstrated for barbituric acid.[43] The computational work sought to establish the stability of the AH and Hy2 experimental crystal forms relative to other possible structures, thus investigating the disorder observed in the Hy2 structure and the relative stability difference of the hydrate and anhydrate phase. The relative humidity dependence of the phase change between Hy2 and AH and the temperature/composition phase diagram are also determined. Hence we provide a complete stability picture, including a variety of new thermo-physical data, of this complex hydrate/anhydrate system, which should be useful in the design of an industrial production process.

2. MATERIALS AND METHODS

2.1. Materials and Preparation of the Forms/Mixtures. Anhydrous PhG (purity ≥99.0%) was purchased from Sigma-Aldrich. A phase pure Hy2 sample was obtained by crystallizing the compound from a hot saturated water:ethanol (1:1) solution. The solution was filtered, cooled to 8 °C, and allowed to crystallize. AH was prepared by drying the Hy2 in a drying oven at 100 °C for about 5 h.

2.2. Polarized Light and Hot-Stage Microscopy. For thermo-microscopic investigations, a Reichert Thermovar polarization microscope equipped with a Kofler hot-stage (Reichert, Vienna, A) was used. Microphotographs were taken with a digital camera (Color View IIIu, Olympus Optical Co. Ltd., Vienna, A). The PhG Hy2 morphologies were observed under a Hirox KH-7700 3D video microscope (Hirox Co. LTD, Japan).

2.3. Differential Scanning Calorimetry and Thermogravimetric Analysis. DSC thermograms were recorded on a DSC 7 or Diamond DSC equipped with a Controlled Cooling Accessory (CCA 7), operated with the Pyris2.0 software (Perkin-Elmer, Norwalk, CT, USA). A few milligrams of accurately weighed (Mettler UM3 ultramicrobalance) sample were heated in perforated Al-pans or sealed, gold plated stainless steel high-pressure capsules (30 μL). For the construction of the temperature/composition phase diagram, different Hy2−AH mixtures were prepared by dehydrating Hy2 samples isothermally at 40 °C in a TGA oven until a desired mass loss was obtained. The samples were transferred to a DSC pan, weighed and sealed. The Hy2−water mixtures were produced by placing precisely weighed amounts of Hy2 and pure water with the aid of a Hamilton syringe and a second accurate weight measurement in a UM3 ultramicrobalance (Mettler, Greifensee, CH) into high-pressure DSC pans. The sealed sample pans were stored for at least 4 h before the DSC runs were started to equilibrate the mixture. AH and Hy2 samples, and Hy2-AH mixtures were heated from 25 to 250 °C at a rate of 5 °C min^{-1} and the Hy2−water mixtures were scanned, after equilibrating for 30 min at room temperature and 5 min at −20 °C, from −20 to 250 °C (5 °C min^{-1}). The two instruments were calibrated for temperature with pure benzophenone (mp 48.0 °C) and caffeine (236.2 °C), and the energy calibration was performed with indium (mp 156.6 °C, heat of fusion 28.45 J $^{1-}$g). The errors on the given temperatures (extrapolated onset temperatures) and enthalpy values are stated as 95% confidence intervals (CIs) based on at least five measurements. TGA was carried out with a TGA7

3962

dx.doi.org/10.1021/jp211948q | J. Phys. Chem. B 2012, 116, 3961−3972

system (Perkin-Elmer, Norwalk, CT, USA) using the Pyris 2.0 Software. Approximately 3 mg of sample was weighed into a platinum pan. Two-point calibration of the temperature was performed with ferromagnetic materials (Alumel and Ni, Curie-point standards, Perkin-Elmer). For dynamic temperature scans, a heating rate of 5 to 10 °C min^{-1} was applied, and dry nitrogen was used as a purge gas (sample purge: 20 mL min^{-1}, balance purge: 40 mL min^{-1}).

2.4. Solution Calorimetry and RH-Perfusion Experiments. The enthalpy of solution ($\Delta_{sol}H$) of Hy2 was measured with the precision solution calorimeter of the TAM III Thermal Activity Monitor (TA Instruments Inc.). The measurement temperature was 25 ± 0.0001 °C, the volume of the vessel was 100 mL, and the stirrer speed was 500 rpm. Four measurements with sample amounts of approximately 300−400 mg were performed. The calorimeter was calibrated with KCl (analytical grade, > 99.5%, Merck). The measured standard solution enthalpy was $\Delta_{sol}H° = 17.51 ± 0.02$ kJ mol^{-1}, which is in agreement with the NIST value of $\Delta_{sol}H° = 17.584 ± 0.017$ kJ mol^{-1}.[44] The TAM Assistant software v0.9 and SolCal version 1.2 was used for the data analysis.

RH perfusion calorimetry experiments were performed with the TAM III nanocalorimeter unit in a 4 mL stainless steel RH perfusion ampule. The relative humidity was controlled with two mass flow controllers, and dry N_2 was used as carrier gas at a constant flow rate of 100 mL h^{-1}. The measurement was performed with 58.9 mg anhydrous PhG and the humidity profile (% RH vs time) was executed as follows: 10% (2.5 h), 20% (5 h), 50% (31.5 h), 20% (1 h). The RH perfusion cell was calibrated with saturated solutions of NaCl (73.5% RH), $Mg(NO_3)_2$ (52.8% RH), and LiCl (11.3% RH). The heat flow of the empty RH perfusion ampule (baseline run with the same humidity steps) was subtracted from the heat flow of the sample measurement.

2.5. Dynamic Moisture Sorption Analysis. Dynamic moisture sorption and desorption studies were performed with the automatic multisample (gravimetric) moisture sorption analyzer (SPS11-10 μ, Project-Messtechnik, Ulm, D). Approximately 60 mg of Hy2 was used for the investigation. The experiment started at 40% RH with a desorption cycle (decreasing humidity) followed by a sorption cycle (increasing humidity) up to 90% RH. In order to assess the dehydration and hydration step with high precision, the RH changes were set to 2% below 40% RH, whereas above this humidity more coarse changes of 10% were chosen.

2.6. Powder X-ray Diffractometry. The powder X-ray diffraction (PXRD) patterns were obtained using an X'Pert PRO diffractometer (PANalytical, Almelo, The Netherlands) equipped with a θ/θ coupled goniometer in transmission geometry, programmable XYZ stage with well plate holder, Cu−K$\alpha_{1,2}$ radiation source with a focusing mirror, a 0.5° divergence slit and a 0.02° Soller slit collimator on the incident beam side, a 2 mm antiscattering slit and a 0.02° Soller slit collimator on the diffracted beam side, and a solid state PIXcel detector. The patterns were recorded at a tube voltage of 40 kV and a tube current of 40 mA, applying a step size of $2\theta = 0.013°$ with 40 s per step in the 2θ range between 2° and 40°. Samples were prepared by mortar and pestle grinding to reduce preferred orientation effects.

2.7. Single Crystal X-ray Diffractometry. A rectangular parallelepiped shaped crystal of Hy2 showing no significant surface features, obtained from slow cooling crystallization from water, was chosen for the single crystal diffraction experiment.

The X-ray data were collected at room temperature (20 °C) on a STOE IPDS-II diffractometer using Mo−Kα radiation ($\lambda = 0.71073$ Å). The structure solution and refinement were carried out using the SIR04[45] and SHELXL97[46] programs incorporated in the WinGX program suite.[47] All non-H atoms were refined anisotropically, and H atoms were located and refined isotropically. The O(1)−H(1) proton and one water proton (H6) are disordered over two positions and both modeled with occupancies of 50:50 each. The disordered H positions of the water molecule were refined by applying geometrical restraints on the H···H distance.

2.8. Computational Generation of the Crystal Energy Landscape. Crystal energy landscapes were generated using the two low energy conformers of PhG, which differ in the mutual orientation of the OH groups,[48] C_{3h} and C_s (Figure 1), held rigid as obtained by ab initio optimization of the isolated molecule structure at the SCF/6-31G(d,p) level of theory using the program Gaussian 03.[49] Using the program CrystalPredictor,[50] 100 000 $Z' = 1$ anhydrate and 500 000 dihydrate crystal structures were randomly generated in 25 space groups, $P1$, $P\bar{1}$, $P2_1$, $P2_1/c$, $P2_12_12$, $P2_12_12_1$, $Pna2_1$, $Pca2_1$, $Pbca$, $Pbcn$, $C2/c$, Cc, $C2$, Pc, Cm, $P2_1/m$, $C2/m$, $P2/c$, $C222_1$, $Pmn2_1$, $Pnna$, $Pccn$, $Pbcm$, $Pmmn$, and $Pnma$. Each crystal structure was relaxed to a local minimum in the intermolecular lattice energy, calculated from the FIT[51] *exp-6* repulsion-dispersion potential and atomic charges that had been fitted to electrostatic potential around the MP2/6-31G(d,p) charge density using the CHELPG scheme.[52] The 15 000 anhydrate and 20 000 hydrate lowest energy structures were reminimized using DMACRYS[53] with a more realistic, distributed multipole model[54] for the electrostatic forces that had been derived using GDMA2[55] to analyze the MP2/6-31G(d,p) charge density. Thus the intermolecular lattice energy (U_{inter}) includes the highly directional electrostatic interactions arising from the lone pair and π electrons.

The optimal proton positions (Figure 1) in all crystal structures within 10 kJ mol^{-1} of the global minimum for the anhydrates and 8 kJ mol^{-1} for the hydrates were determined using CrystalOptimizer.[56] This was done by minimizing the lattice energy (E_{latt}), calculated as the sum of the intermolecular contribution (U_{inter}) and the conformational energy penalty paid for distortion of the molecular geometry to improve the hydrogen bonding geometries. Conformational energy penalties (ΔE_{intra}, with respect to C_{3h}), and isolated molecule charge densities were computed at the SCF/6-31G(d,p) and MP2/6-31G(d,p) levels, respectively, for each conformation considered in the minimization of E_{latt}.

To approximate the polarization of the molecular charge distribution in the crystal, as has been found necessary in CSP studies of peptides,[57,58] the charge density used in the final evaluation of E_{latt} was generated in a dielectric constant, $\varepsilon = 3$, a value typical of organic crystals. Thus, the final MP2/6-31G(d,p) electron density calculations used the polarizable continuum model (PCM)[59] implemented in Gaussian 03. The intramolecular energy penalty ΔE_{intra} was calculated from the SCF energies in the same PCM ab initio calculations, excluding the interaction energy between the molecule and the polarizable continuum.

All calculated hydrate structures were run through the ADDSYM function of PLATON[60] in order to determine the true space group and Z' value. Structural comparisons were made using Mercury,[61] including the evaluation of the difference in the optimal root-mean-square overlay of all non-
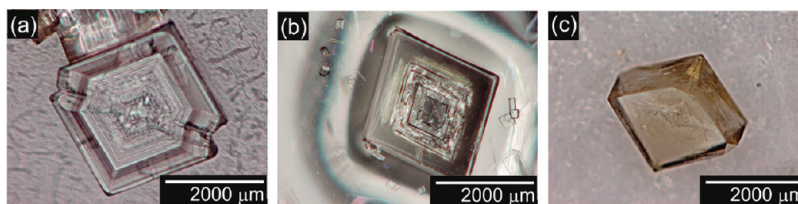
Figure 2. PhG dihydrate crystals representing the range of morphologies: (a) Six-sided crystal exhibiting closed loop spiral growth steps obtained from evaporation from a saturated EtOH:water (1:1) solution at room temperature. (b) Rhombic, plate-like crystal with lozenge-shaped steps obtained from evaporation from a saturated water solution at room temperature. (c) Block-like dihydrate crystal from cooling crystallization of a saturated water solution.

hydrogen atoms in a 15 molecule coordination cluster (rmsd$_{15}$).[62]

3. RESULTS AND DISCUSSION

3.1. Crystallization Results and Crystal Morphology of Hy2. The experimental screen from 26 solvents resulted in the two known solid forms (anhydrate and dihydrate[63]), and novel solvates from methanol and dimethyl sulfoxide. The methanol solvate is unstable and transforms quickly to the anhydrate if removed from the mother liquor. By contrast, the dimethyl sulfoxide solvate is stable at ambient conditions. This solvate shows an inhomogeneous melting process (a peritectic/melting decomposition of the solvate that overlaps with the crystallization of the anhydrate) at 87 °C upon heating.

The surface features and morphology of the Hy2 crystals were observed to depend on the solvent and crystal growth temperature (as previously reported[33]). Solvent evaporation experiments predominantly gave rhombic and six-sided plates exhibiting characteristic spiral growth steps, i.e., lozenge-shaped steps on the rhombic plates or rhombic to six-sided shaped steps on the six-sided plates (Figure 2). Slow cooling crystallization experiments predominantly gave rhombic to rectangular shaped plates or blocks with no surface features. Nevertheless, all Hy2 batches obtained showed identical IR spectra.

3.2. Moisture Sorption Experiments. The moisture sorption/desorption isotherm of PhG (Figure 3) shows that the anhydrate is stable (i.e., does not absorb water) up to 32% RH. At higher moisture conditions, the sample takes up water, and the transformation to Hy2 occurs. The measured mass gain of 27.9% corresponds to 1.95 mol water, which is only slightly

Figure 3. Moisture sorption and desorption curves of PhG Hy2/AH at 25 °C. The circles present data points that fulfill the present equilibrium condition (mass change), whereas crosses mark measurement values that did not reach the equilibrium within the allowed time limit (100 h).

below the theoretical value of 2 mols of water per mole of PhG (28.6% referred to the anhydrous mass). On decreasing the humidity, the dehydration to AH occurs when the RH is less than 16%. The distinct steps and hysteresis between the sorption and desorption isotherms are characteristic for a stoichiometric hydrate, but the hysteresis in the PhG system is rather small compared to 2,4-dihydroxybenzoic acid hemihydrate[11] and aripiprazole monohydrate.[64] The sorption/desorption isotherms show that Hy2 is a very stable hydrate, which releases its water only at low relative humidities, and conversely the AH is a rather unstable anhydrate phase, which absorbs water (moisture) above 32% which is below ambient conditions (40 to 60% RH). This information is crucial for handling of the AH, and therefore all experiments performed on the AH were done with samples that had been stored over a desiccant.

3.3. Crystal Structures. The single X-ray crystal structure of the anhydrate deposited in the CSD as PHGLOL01[40] was used for structural comparisons. The PhG molecule is essential planar, C_{3h} point symmetry, with the OH protons slightly out of plane of the benzene ring forming more linear hydrogen bonds. The molecules pack in a folded molecular aggregation pattern, consisting of almost perpendicular hydrogen-bonded planes.

Hy2 crystallizes in the orthorhombic space group *Pnma* with half a PhG and one water molecule in the asymmetric unit. [**Crystal data of Hy2**: $C_6H_6O_3 \cdot 2(H_2O)$, M_r = 162.14, orthorhombic, space group *Pnma*, T = 20(2) °C, size [mm]: 0.35 × 0.3 × 0.1, a = 6.6209 (17) Å, b = 13.561 (3) Å, c = 8.0462 (15) Å, V = 722.4 (3) Å^3, Z = 4, ρ_{calc} = 1.491 Mg m^{-3}, 4393 reflections measured, 732 independent reflections, 650 observed reflections, θ range for data collection: 2.94 − 26.05 h, k, l, range: −8 < h < 8, −15< k < 16, −8 < l < 9, data: 732, restraints: 2, parameters: 81, $R[F^2 > 2\sigma(F^2)]$ = 0.037, $wR(F^2)$ = 0.093, R int =0.037, Goodness of fit on F^2= 1.10, $\Delta\rho_{max}$ = 0.23, $\Delta\rho_{min}$ (e Å^{-3}) = −0.24.] The stoichiometry is in agreement with the moisture sorption/desorption (section 3.2) and TGA results (section 3.5) as well as previous structure determinations.[17,34,35] The average X-ray structure[35] exhibits a mirror plane located down center of the benzene ring of the PhG molecule (Figure 4a), which dictates a 50:50 positional disorder of one of the three HO protons, and, consequently, one of the water protons is also 50:50 disordered over two positions. In contrast to the AH structure, the Hy2 OH protons are nearly coplanar with the benzene ring (max. deviation from planarity <5°), forming almost linear hydrogen bonds. The PhG molecules are linked by O−H⋯O hydrogen bonds through the water molecules, with each of the three PhG OH groups forming two hydrogen bonds with water and each water molecule forming three hydrogen bonds: two with PhG and one with an adjacent water molecule. The strongly hydrogen-bonded PhG and water molecules form corrugated layers
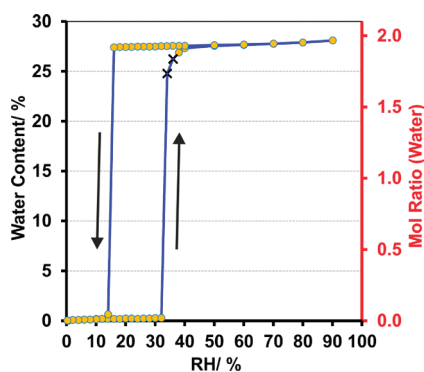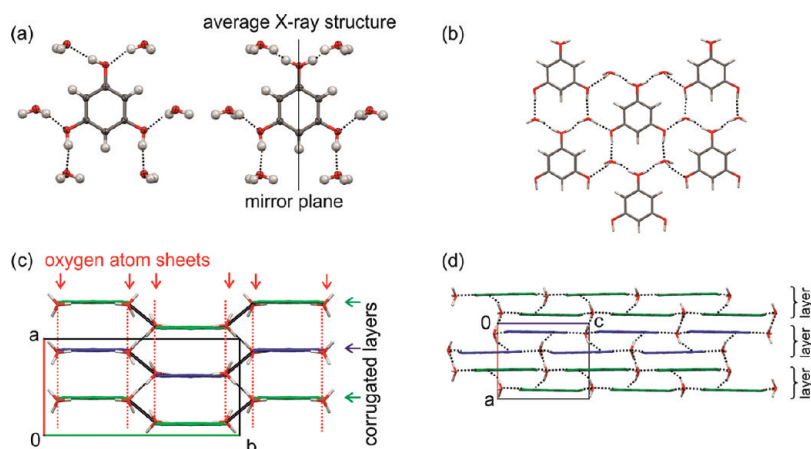
Figure 4. (a) Left: PhG water complex, showing the hydrogen bonds on a local level; Right: proton disorder as observed from the average X-ray structure. (b) One hydrogen bonded layer of the structures as seen in projection on (100). (c) Structure of PhG dihydrate projected along [001], showing the corrugated layers formed by the PhG molecules (indicated in green and blue) and sheets of oxygen atoms (red dotted lines). (d) Dihydrate structure projected along [010].

parallel to (100). The corrugated layers, as defined by Wallwork and Powell[17] and Singh and Singh,[33] are formed by the PhG/water molecules located at $x \sim 1/8$ and $x \sim 3/8$, and the PhG/water molecules at $x \sim 5/8$ and $x \sim 7/8$, respectively (Figure 4b and c). All molecular interactions involving the PhG OH groups are within one layer. The hydrogen bond formed between a pair of water molecules links the different layers (Figure 4d). Compared to the high number of interactions within each corrugated layer (six hydrogen bonds for each PhG molecule), the interlayer interactions involve only water···water interactions. All PhG molecules within one layer point in the same direction along [001]. There is an alternative set of layers defined by the molecules at $x \sim 5/8$ and $x \sim 3/8$ (Figure S2, Supporting Information), with the PhG molecules in different orientations. Interactions within the layer are through water molecules and the interlayer interactions through a water···PhG interaction. Perpendicular to either definition of layers, parallel to (010), there are sheets of oxygen atoms, formed of water and PhG oxygens (Figure 4c), and each sheet is linked through O—H···O hydrogen bonds to an adjacent sheet. PhG and water oxygen atoms within the same sheet but different layers have approximately the same y and z coordinates and differ in their x coordinates by approximately $a/2$ (Figure 4c).[17,33]

3.4. Crystal Energy Landscapes. *Comparison of Computed and Experimental Anhydrate Structures.* The lattice energy landscape of the PhG anhydrate (Figure 5a, Table 1) has two structures that are more stable than any others, both of which correspond to the experimental structure if proton positions are ignored. The most stable structure overlays a 15-molecule coordination sphere with an rmsd_{15} of 0.39 Å including the hydrogen atoms. The other low energy structure has the same packing of all C and O atoms (Figure 5b), but differs in some proton positions, giving a different C_s molecular symmetry and different space group ($Pna2_1$ instead of $P2_12_12_1$). The two structures exhibit the same intermolecular interactions, differing in the directionality of the O—H···O hydrogen bonds (Figure 5b), with the deviation of the polar hydrogen atoms from planarity well reproduced by the modeling technique. The small lattice energy difference and iostructurality of the calculated structures indicates that proton disorder cannot be excluded as domains of the alternate structure may exist within
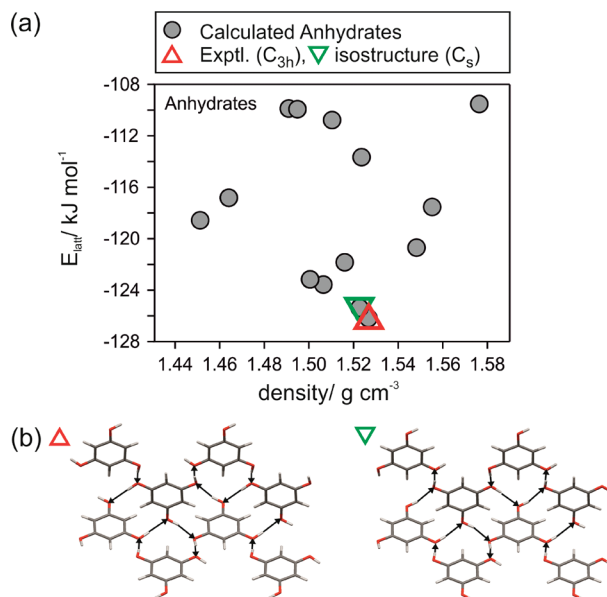

Figure 5. (a) Lattice energy landscapes of the PhG anhydrate. Each symbol denotes a crystal structure (Table 1). (b) Hydrogen bonding of the calculated experimental (A_C3h_1) and second lowest calculated structure (A_Cs_3), showing the isostructurality apart from some hydroxyl protons.

the known form. However, the X-ray diffraction studies[18,40] did not report any proton disorder or diffuse scattering.

The calculated AH lattice energy of -126.2 kJ mol^{-1} is in good agreement with de Wit et al.'s[65] experimentally determined heat of sublimation of 127.9 kJ mol^{-1} using a torsion-effusion technique and 126.0 kJ mol^{-1} by mass loss effusion, measured in the temperature range of 100 to 133 °C. Since the lattice energy corresponds to infinitely separating the molecules in a static crystal at absolute zero (-273 °C), the agreement implies that the empirical parametrization of the repulsion—dispersion potential has partially absorbed the thermal (heat capacity) and crystal zero-point energy effects.[66]

Comparison of Calculated and Experimental Dihydrate Structures: Proposed Domain and Stacking Fault Structure. The PhG dihydrate lattice energy landscape (Figure 6a) shows a much higher density of favorable structures than for the

Table 1. Comparison of the Experimental and Selected Computed AH and Hy2 Structures of PhG[a]

ID[b]	space group[c]	a/ Å	b/ Å	c/ Å	γ/ °	density/gcm⁻³	U_{inter}/kJ mol⁻¹	E_{latt}/kJ mol⁻¹	rmsd₁₅/Å[f]
				PHGLOL01 (Experimental AH Structure)					
exptl.	$P2_12_12_1$	4.778	9.358	12.443	90	1.484	−	−	0
			Computationally Generated Low Energy PhG Anhydrate Structures						
A_C3h_1	$P2_12_12_1$	5.084	9.196	11.834	90	1.527	−129.41	−126.18	0.36
A_Cs_3	$Pna2_1$	11.901	5.067	9.123	90	1.523	−130.56	−125.38	0.32
A_C3h_13	$Pna2_1$	8.592	12.189	5.310	90	1.506	−127.13	−123.57	−
A_Cs_4	$Pca2_1$	12.177	5.358	8.556	90	1.500	−128.94	−123.17	−
A_C3h_171	Pa	8.906	11.800	5.150	91.6	1.548	−124.15	−120.70	−
				PhG-Hy2 (Experimental Hy2 Structure)					
Exptl.	$Pnma$	6.621	13.561	8.046	90	1.491	−	−	0
			Computationally Generated PhG Dihydrate Structures						
				Group A					
H_Cs_1613	$P2_12_12_1$[d]	6.422	13.438	7.862	90	1.587	−272.91	−266.26	0.17
H_Cs_6	$Pn2_1a$[d]	6.405	13.442	7.882	90	1.587	−271.83	−265.49	0.12
H_C3h_4696	$P2_12_12_1$[d]	6.439	13.360	7.915	90	1.582	−266.76	−261.73	0.14
H_Cs_14	$P2_12_12_1$[d]	6.485	13.113	8.043	90	1.575	−267.70	−259.61	0.16
				Group B					
H_Cs_29	$P112_1/b$[e]	6.374	13.978	7.877	105.4	1.592	−272.00	−265.70	0.21
H_Cs_27	$I11b$[e]	6.369	13.971	7.890	105.5	1.592	−271.61	−265.48	0.20
H_C3h_19	$P112_1/b$[e]	6.438	13.658	7.929	102.2	1.580	−266.49	−262.02	0.18
H_Cs_64	$I11b$[e]	6.506	13.418	8.060	76.9	1.572	−264.06	−256.57	0.17

[a]A full list of the structures shown in Figures 5 and 6 is given in the Supporting Information (Tables S3 and S4). [b]ID: Experimental (exptl.) and identification codes for the computed structures. [c]Nonstandard space groups settings were chosen to show the similarity in lattice parameters. [d]Proton ordered, Z' = 1 space group, which Platon ADDSYM classifies as $Pnma$ Z' = 0.5. [e]Proton ordered, Z' = 1 space group, which PLATON ADDSYM classifies as $C2/c$ Z' = 0.5. [f]The optimal 15-molecule coordination cluster overlay with the experimental structure (non-hydrogen atoms only).
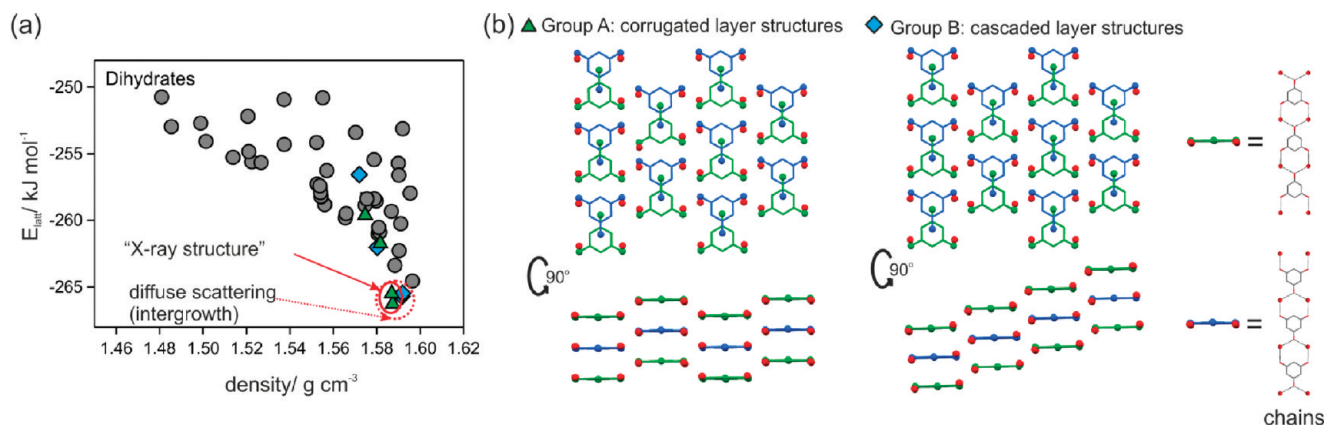

Figure 6. (a) Lattice energy landscape for PhG dihydrate. Each symbol denotes a crystal structure (Tables S4, Supporting Information). Green triangles: structures that match all non-hydrogen atoms with the experimental structure (Table 1, group A); blue diamonds: match two stacks of adjacent PhG water chains of the experimental structure (Table 1, group B); gray dots: structures with just the same infinitive linear chains as experimental structure. The red ellipsoid encompasses proton-ordered versions of the proton-disordered X-ray structure, the red dotted circle encloses the structures that may account for the diffuse scattering effects. (b) Packing comparison between group A and B structures, defined in Table 1. Proton positions are omitted for clarity. PhG molecules, forming the corrugated/cascaded layers are shown in the same color.

anhydrate (Figure 6), but all low-energy dihydrate structures contain the same infinitive linear chains (Figure 6b, right). The experimental structure is the most stable, but there are two groups of low energy structures (groups A and B, Table 1) which are closely related to the experimental structure. The hydrogen boding motifs are identical for these eight structures if the directionality of the O−H···O hydrogen bonding is ignored (Figure 7).

Four of the low energy structures (group A, Table 1, Figure 6), including the global minimum, show the packing observed in the experimental Hy2 structure, (i.e., carbon and oxygen atom positions are essentially the same,) although three of

these structures have the C_s proton conformation, and all differ in the directionality of the O−H···O hydrogen bonds (Figure 7). Only the two most stable group A structures exhibit PhG and water OH proton positions observed as the disorder components of the experimental structure[34,35] (Figure 4b). The difference between these two lowest-energy group A structures is the directionality of every alternate O(1)−H···O hydrogen bond, leading to $P2_12_12_1$ and $Pna2_1$ space groups. These two group A structures correspond to the two structures that Thomas et al.[35] derived as starting points for periodic quantum mechanical calculations. The other two less stable group A structures (both space group $P2_12_12_1$, ΔE_{latt} < 7 kJ mol⁻¹ with
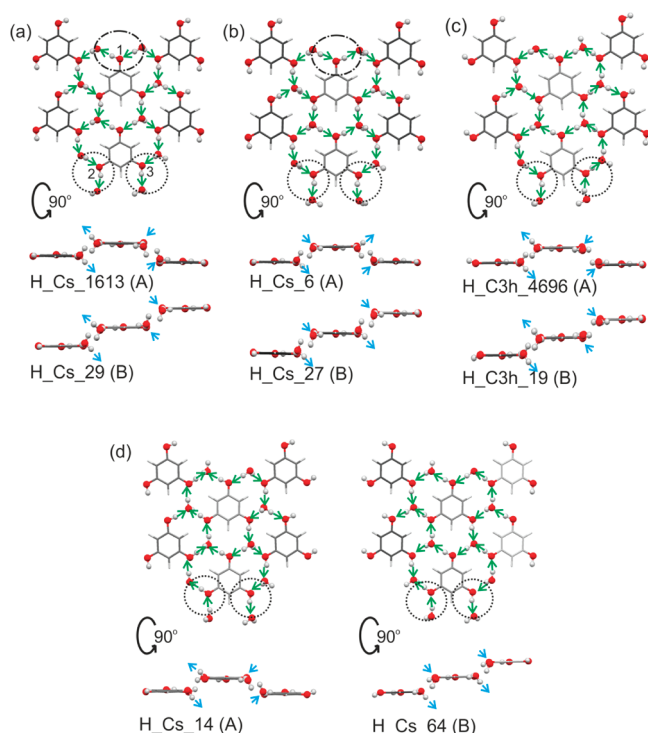
Figure 7. Hydrogen bonding connectivity (within one layer) of the four group A and B dihydrate structures related to the experimental PhG dihydrate: (a) H_Cs_1613 and H_Cs_29, (b) H_Cs_6 and H_Cs_27, (c) H_C3h_4696 and H_C3h_19, and (d) H_Cs_14 and H_Cs_64. Hydrogen bonding directionality is indicated with arrows along the covalent O−H bond: green − within layers; blue − in between layers.

respect to most stable Hy2) differ in the O(2)H and O(3)H proton positions from those determined in the X-ray diffraction experiment.[35] These two higher energy structures cannot be ignored in discussions of possible proton disorder. Checking for higher (pseudo)symmetry using Platon[60] showed that all four group A structures can be expressed as proton disordered *Pnma* structures. The two lowest-energy group A structures show in their common maximal nonisomorphic supergroup (*Pnma*) the 50% occupancy proton disorder in the (average) experimental X-ray Hy2 structure. On a local level, the proton must adopt one position, and this will determine the hydrogen bonding directionality, resulting in $P2_12_12_1$ and $Pna2_1$ domains within the crystal.[35]

Four other calculated low energy structures (group B, Figure 6) have the same sheets of oxygen atoms as group A (Figure 4c). The two groups differ in the displacement of half of the oxygen sheets by $a/2$, leading to cascaded hydrogen-bonded layers in group B structures in contrast to the corrugated hydrogen-bonded layers present in group A (Figure 6b). If one sheet of oxygen molecules is displaced by $a/2$ with respect to the other, the oxygen atoms of the displaced sheet are still in a position that allows them to form the same number of strong hydrogen bonds with the oxygen atoms of the adjacent sheet. This is possible because the PhG oxygen atoms take approximately the same position as the water oxygen atom, and vice versa. Such a displacement of oxygen sheets would also give rise to diffuse scattering effects in X-ray diffraction experiments.[17,33] The similarities in structure and energy of the group A and group B structures imply a high probability of stacking-fault-like defects of the oxygen sheets and possible

intergrowth of group A and group B domains, illustrated in Figure 8, as observed for aspirin,[67,68] in addition to the $P2_12_12_1$ and $Pna2_1$ domains within group A. The intergrowth of group A and group B domains (Figure S8, Supporting Information) adds the range of possible proton positions to the defect structure anticipated by Wallwork and Powell[17] and Singh and Singh[33] from the experimental Hy2 structure. The ortho-rhombic packing motif (group A) seems to be preferred for PhG Hy2, as none of the crystallization experiments resulted in a phase where the monoclinic domains (group B) dominated the structure.
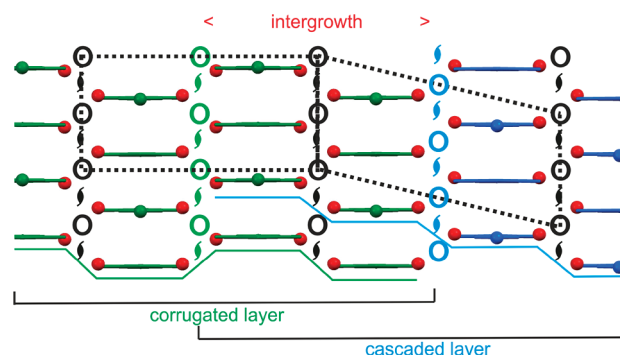

Figure 8. Hypothetical packing of PhG dihydrate showing the possible intergrowth of corrugated and cascaded layers. Selected symmetry elements are shown: black − in common to both layers; green − for the corrugated layers in the $P2_12_12_1$ and $Pna2_1$ group A structures that have *Pnma* symmetry if proton positions are ignored; blue − for the cascaded layer in the $P2_1/c$ and *Cc* group B structures which have $C2/c$ symmetry if proton positions are ignored. Orthorhombic and monoclinic unit cells are indicated with dotted lines.

Powder X-ray Diffraction Differences Resulting from Stacking Defects. We have compared the PXRD measurements of Hy2 batches obtained from different solvents and crystallization rates with the simulated powder patterns of the computer generated structures. Figure 9a contrasts the PXRD pattern for Hy2 produced by crystals obtained from cooling crystallization (sample 1, did not possess any significant surface features) with that of crystals obtained from solvent evaporation from a Petri dish (sample 2, irregular six sided platelet with spiral steps). Several of the diffraction peaks are broadened in the pattern of sample 2 but sharp for sample 1. The most notable differences are in reflections originating from the (111) and (121) planes, which are formed by PhG oxygen (Figure 9b) and water oxygen atoms (Figure 9c). The experimental powder pattern for sample 1 (the slow crystallization product) is in good agreement with those of the group A crystal structures. The only differences in the powder patterns arise from the temperature disparity (thermal expansion), while the impact of the proton disorder is negligible. Similarly, as discussed in the Supporting Information, varying proportions of the stacking faults described by Figure 8 are compatible with the variations in the powder patterns.

3.5. Hydrate/Anhydrate Phase Transformation. The dehydration process of Hy2 between 55 and 90 °C, as observed with HTM (Figure 10), is governed by a nucleation and growth mechanism, which is indicated by the appearance and growth of dark spots upon heating. These spots, emerging at the surface and macroscopic defects of the Hy2 crystals, represent the nucleation centers of the AH. Although the number of the
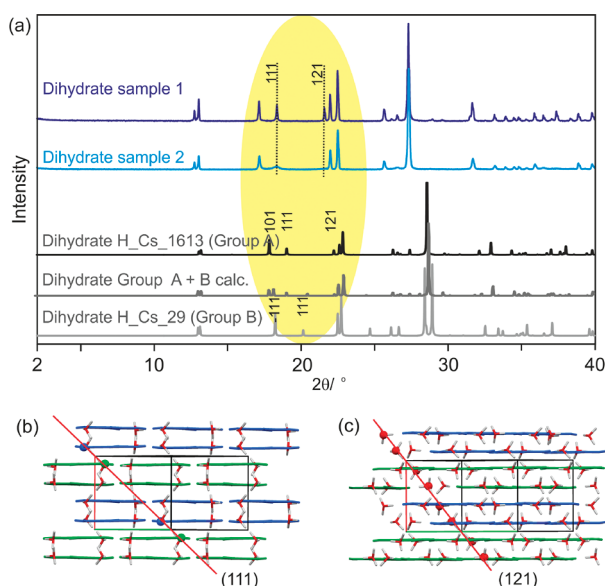
3967

dx.doi.org/10.1021/jp211948q | *J. Phys. Chem. B* 2012, 116, 3961−3972

Figure 9. (a) Experimental PXRD patterns for different PhG dihydrate crystallization batches (sample 1: cooling crystallization from water; sample 2: solvent evaporation from ethanol) contrasted with the simulated patterns of a computationally generated group A and group B dihydrate structures (Table 1) and of a P1 cell corresponding to a combination of the two structures (group A+B, Figure 8). Note that the computationally generated structures are perfectly ordered structures and therefore exhibit no diffuse scattering. The area highlighted in yellow shows the key differences corresponding to the packing diagrams showing (b) the (111) and (c) the (121) planes. Oxygen atoms lying on the planes are shown as balls.

nucleation centers increases with temperature, the overall dehydration process is dominated by the high growth rate of a limited number of nuclei. The process results in the formation of aggregates of homogeneously sized AH crystals (<10 μm) with the original shape of the Hy2 crystals (called "pseudomorphosis"), which is characteristic for the desolvation of stoichiometric solvates. Condensation and sublimation of the AH begins at temperatures above 150 °C. Between 217 and 220 °C, the sublimed AH crystals decompose and melt. By embedding the Hy2 crystals in high viscosity silicon oil and applying a heating rate of about ~10 °C min^{-1}, the incongruent melting (peritectic decomposition) of the Hy2 can be determined at 118 − 120 °C. At this temperature, the Hy2 crystals fuse partially, and at the same time nucleation and growth of AH occurs, accompanied by the release of water vapor as indicated by the formation of bubbles. All dehydration

experiments resulted in only one anhydrous phase (AH), which was confirmed by IR-spectroscopy and/or PXRD.

The removal of the water from Hy2 is connected with a disruption of all O−H⋯O hydrogen bonds and rearrangement of the PhG molecules. The observed nucleation at the surface and macroscopic defects is likely to be associated with the escape of the water. The considerable rearrangement of the PhG molecules into the anhydrate structure could be relatively facile, as it can be simulated by lattice energy minimization from the dihydrate structure with the water molecules computationally removed and a proton transferred to give a C_{3h} conformation (Figure 11).
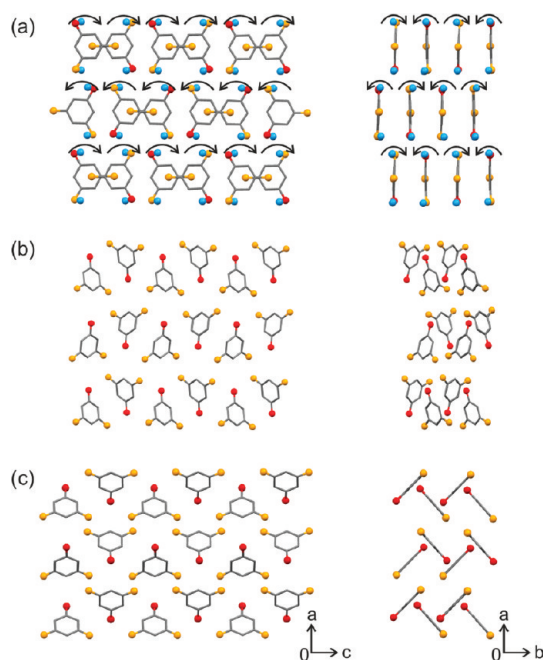

Figure 11. A model for the rearrangement of the PhG dihydrate structure to the anhydrate after computational removal of water molecules. (a) PhG dihydrate, with arrows indicating the direction of movement of the molecules when the water molecules (position indicated in blue) are removed and the resulting lattice energy minimized; (b) an intermediate structure emphasizing the tilting of the molecules; and (c) the anhydrate structure that results. The structures are orientated with respect to the axes shown of the anhydrate structure. Oxygen atoms are colored differently for clarity. Hydrogen atoms are omitted, but the simulation form required the C_{3h} molecular geometry (C3h_4696, Table 1).
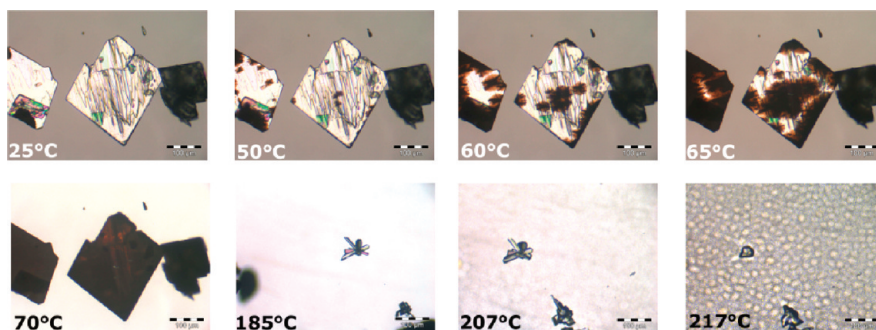

Figure 10. Photomicrographs (dry preparation) of the dehydration process of PhG dihydrate.

3968

dx.doi.org/10.1021/jp211948q | J. Phys. Chem. B 2012, 116, 3961−3972

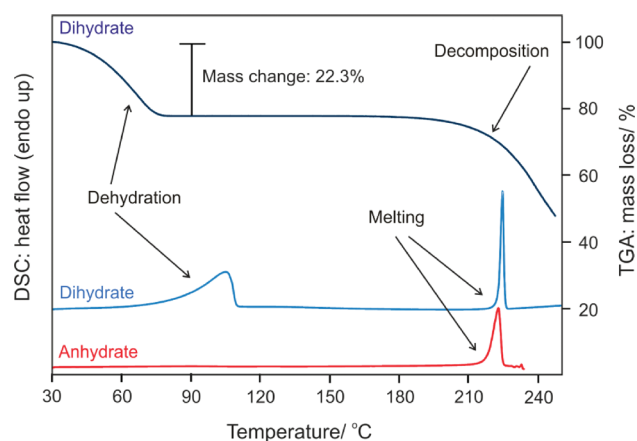The TGA curve of Hy2 shows (Figure 12) a one-step dehydration process, which corresponds to the loss of 2 mols of

Figure 12. DSC and TGA thermograms of PhG anhydrate and dihydrate (pin-holed sample pans and a heating rate of 5 °C min⁻¹ was used for all thermograms).

water per PhG molecule (measured mass loss: 22.3%, theoretical value for 2 mols water relative to the hydrate is 22.22%). The second step observed in the TGA curve occurring around the melting temperature of AH corresponds to the decomposition of the PhG. In a pin-holed DSC capsule, the dehydration process of Hy2 is observed as a broad endothermic peak, followed by the melting process of AH at 221 °C. The DSC curve of the AH exhibits only the melting process, indicated by an endothermic peak with a heat of fusion ($\Delta_{fus}H_{AH}$) of 34.4 mol⁻¹. The decomposition process that starts before melting of the AH does not produce a strong change in the DSC signal, and so the thermolysis (thermal decomposition) will contribute to the wide range of AH melting points reported in textbooks,[69] the Beilstein reference database,[70] and other literature sources.[71] One can also find melting points of PhG reported in the range from 113 to 118 °C, which corresponds to the peritectic decomposition range of Hy2 and not the melting point of the anhydrous substance.

3.6. Phase Diagram of the PhG/Water System. The temperature/composition phase diagram of PhG/water (Figure 13) shows the typical behavior of an incongruent melting hydrate with a peritectic temperature at 120 °C and a eutectic (monotectic) between Hy2 and water at 0 °C. The peritectic temperature (<120 °C, at roughly ambient pressure) may be defined as the temperature up to which a hydrate is thermodynamically stable in the presence of its own saturated solution and vapor pressure. Thus a slurry (suspension) of the hydrate in water would contain only anhydrous PhG above 120 °C.

3.7. Enthalpy of Hydrate/Anhydrate Transition. The enthalpy of the Hy2/AH transition can be estimated from the results in Table 2. The dehydration process, $\Delta_{dehy}H_{Hy2\text{-}AH}$, measured in open DSC pans (pin holed lid, Figure 12), can be subdivided (application of Hess's law) into the enthalpy of hydrate to anhydrate transformation, $\Delta_{trs}H_{Hy2\text{-}AH}$, and the vaporization of the expelled water.

$$\Delta_{trs}H_{Hy2\text{-}AH} = \Delta_{dehy}H_{Hy2\text{-}AH} - 2\Delta_{vap}H_{H2O} \quad (1)$$

If we subtract the known enthalpy value for the vaporization of water at the dehydration temperature (onset, $T_{dehy} \sim 75$ °C
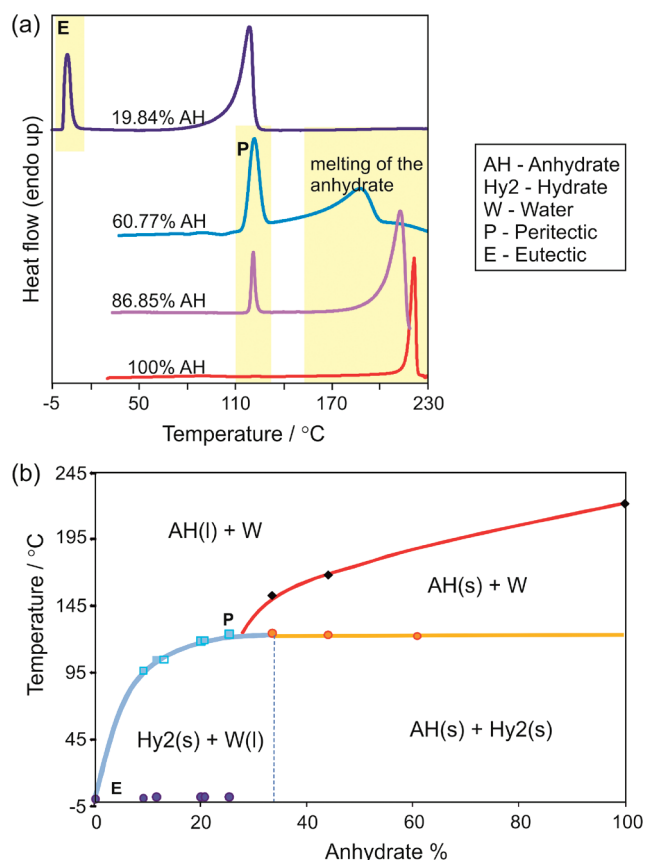

Figure 13. (a) Selected DSC thermograms of the PhG−water system (sealed capsules and heating rates of 5 °C min⁻¹ were applied) used for the construction of the (b) temperature/composition phase diagram.

at which $\Delta_{vap}H°_{H2O} = 41.81$ kJ mol⁻¹)[72] from the measured enthalpy of dehydration according to eq 1, we can estimate the enthalpy of the hydrate to anhydrate phase change as 19.3 kJ mol⁻¹.[73]

With isothermal calorimetry ($T = 25$ °C, RH-perfusion cell) an enthalpy of hydration ($\Delta_{hy}H_{AH\text{-}Hy2}$) of −107.04 kJ mol⁻¹ was obtained. Since the magnitude of the heat of condensation of water ($\Delta_{cond}H_{H2O}$) is equal to the heat of vaporization, we can use eq 2 to calculate the transition energy of AH to Hy2 ($\Delta_{trs}H_{AH\text{-}Hy2}$):

$$\Delta_{trs}H_{AH\text{-}Hy2} = \Delta_{hy}H_{AH\text{-}Hy2} - 2\Delta_{cond}H_{H2O} \quad (2)$$

Using a value of $\Delta_{vap}H°_{H2O}$ (25 °C) = 43.99 kJ mol⁻¹ = $-\Delta_{cond}H°_{H2O}$ (25 °C)[72] gives a transition energy of −19.1 kJ mol⁻¹, which is in excellent agreement with the value obtained from DSC experiments (19.3 kJ mol⁻¹) measured at a higher temperature. The order of magnitude of the experimental enthalpic transition energy is in the range of values measured for other stoichiometric dihydrates.[42,43]

The simplest estimate for the hydrate to anhydrate transition is to calculate $\Delta U_{Hy2\text{-}AH}$ from AH, Hy2, and ice lattice energies, E_{latt}.

$$\Delta U_{Hy2\text{-}AH} = -E_{latt}(Hy2) - (-E_{latt}(AH) - 2E_{latt}(ICE))$$

$$\approx \Delta_{trs}H_{Hy2\text{-}AH} \quad (3)$$

Using the lattice energy of the experimental structures (the global anhydrate and hydrate search minima (Table 1)) and the

Table 2. Thermodynamic Data for PhG Anhydrate and Dihydrate

Phase	Anhydrate (AH)	Dihydrate (Hy2)
melting point (T_{fus}), °C		
hot-stage microscopy	217−220[a]	
differential scanning calorimetry (onset)	221 ± 2	
enthalpy of fusion ($\Delta_{fus}H$), kJ mol^{-1}	34.4 ± 0.5	
peritectic decomposition ($T_{diss,Hy2}$), °C		
hot-stage microscopy		118−120
differential scanning calorimetry (onset)		119.2 ± 0.3
enthalpy of dehydration ($\Delta_{dehy}H$), kJ mol^{-1} at ∼70 °C (DSC, open pan)		103.0 ± 0.3
enthalpy of hydration ($\Delta_{hy}H$), kJ mol^{-1} at 25 °C (RH-Perfusion)		−107.0
enthalpy of solution ($\Delta_{sol}H$) in water at 25 °C, kJ mol^{-1} (solution calorimetry)		39.7 ± 1.4
lattice energy (E_{latt}), kJ mol^{-1}	−126.18	−266.26[b]
enthalpy of transition ($\Delta_{trs}H$), kJ mol^{-1}		
differential scanning calorimetry, 75 °C		19.3 (Hy2 → AH)
RH-perfusion (isothermal calorimetry), 25 °C		−19.1 (AH → Hy2)
lattice energy calculations, −273 °C		20.0−25.0 (Hy2 → AH)

[a]Melting and decomposition occur in the same temperature range at the heating rates applied. No detailed experimentation was carried out to study the thermal decomposition and its impact on the melting temperature and heat of fusion. [b]Lattice energy calculated for the proton ordered Hy2 structure.

energy range for the ordered ice polymorphs[74−80] ($E_{latt(ICE)}$ = −57.54 to −60.02 kJ mol^{-1}, Supporting Information Table S2) gives ΔU_{Hy2-AH} of 20.0 to 25.0 kJ mol^{-1}. This confirms that hydrate formation is driven by a greater potential energy. The experimental measurements and computational estimates compare the separation of the hydrate into anhydrate and water into different phases at different temperatures. Computationally, we break the hydrate into infinitely separated anhydrate and water molecules (ideal gas) at absolute zero (−273 °C), neglecting thermal contributions and zero-point vibrational effects. In contrast, experimentally we transform the hydrate into solid anhydrate and water vapor, assuming that water evaporates from the liquid state. The experimental thermodynamic arguments are complicated by consideration of whether the heat of vaporization of water or the heat of sublimation of ice are more appropriate, influenced by whether the water within the hydrate structure is isolated or liquid-like.[81]

The transition enthalpy of hydrate to anhydrate can, in theory, also be calculated from the differences of the heats of solution ($\Delta_{sol}H$, eq 3) of AH and Hy2:

$$\Delta_{trs}H_{AH-Hy2} = \Delta_{sol}H_{AH} - \Delta_{sol}H_{Hy2} \qquad (4)$$

For Hy2 we measured a $\Delta_{sol}H_{Hy2}$ of 39.7 ± 1.4 kJ mol^{-1}; however, a meaningful determination of $\Delta_{sol}H$ by solution calorimetry in water for AH was not possible, since the transformation of AH to Hy2 is too rapid. We can estimate $\Delta_{sol}H_{AH}$ by the use of the $\Delta_{trs}H_{AH-Hy2}$ value obtained with the RH perfusion technique and application of eq 3 (see also Supporting Information, Figure S4) as approximately 21 kJ mol^{-1} at 25 °C. The rate of conversion is affected by surface area and macroscopic defects. The crystallographic disorder is associated with sufficiently similar water environments within the crystal and very small energy differences (by calculation). Hence we would not expect the crystallographic disorder to affect rate and dehydration, which was consistent with any difference being far too subtle to be detected by the analytical methods.

4. CONCLUSIONS

The experimental search for solid state forms of PhG has resulted in only two practically relevant solid phases: the dihydrate and anhydrate. A highly metastable methanol solvate and a dimethyl sulfoxide solvate that could arise in processing phloroglucinol have also been detected. The dihydrate crystallizes with a range of morphologies and surface features.[33]

Confidence that all stable anhydrate and dihydrate forms have been found is provided by the crystal energy landscapes which have the experimental anhydrate and a proton ordered version of the dihydrate as the global minima in lattice energy. These landscapes show that closely related structures are so similar in energy, well within the likely energy range for possible polymorphs,[82] that they can account for the proton disorder and stacking faults in the dihydrate. These two groups of low-energy Hy2 structures provide a valuable starting point for further disorder modeling and experiments to explain the complex diffuse scattering in the hydrate. The layer models giving rise to the diffuse scattering proposed by Wallwork and Powell[17] and Singh and Singh[33] may therefore be improved upon on a molecular scale by a combination of the local ordering suggested by Thomas et al.[35] (group A) and the layer intergrowth models (groups A and B) proposed here.

Anhydrous PhG rapidly absorbs water above 32% RH, making handling difficult. The dihydrate loses water below 16% RH, and this relatively small hysteresis, close to ambient conditions, makes this otherwise straightforward hydration behavior practically problematic. The temperature/composition phase diagram under saturated water vapor pressure, the thermal desolvation behavior, and the moisture sorption/desorption studies provide the thermodynamic and kinetic data needed for controlling the handling, processing, and storing of PhG. The dihydrate is enthalpically stabilized by approximately 19 kJ mol^{-1} as derived from two experimental approaches. Monitoring the loss of water by thermal microscopy revealed that nucleation was associated with macroscopic defects on the surface, consistent with the loss of water not being significantly affected by the stacking faults/domains and surface morphology variations, and the relationships between the crystal structures at the atomic level.

This novel experimental and computational strategy has provided deeper understanding of this hydrate system, with a reassuring consistency between the different techniques. PhG represents another example where the computed crystal energy landscape calculations can assist in proposing feasible models for the experimentally observed disorder.[83−85] In this case, the small energy differences between structures differing only in polar proton positions adds to the confidence that the nature of the disorder, both in proton position and stacking defects, does not affect the processing.

■ ASSOCIATED CONTENT

Ⓢ Supporting Information
Polymorph screen, Fourier-transform infrared spectroscopy, illustration of the alternative definition of experimental Hy2

layers, PXRD comparison of calculated $P2_12_12_1$ and $Pna2_1$ structures, conformational analysis of phloroglucinol, representation of the experimental structures and ice polymorphs, computationally generated crystal energy landscape, and calculated group A and B hydrate structures. This information is available free of charge via the Internet at http://pubs.acs.org/.

■ AUTHOR INFORMATION

Corresponding Author
*E-mail: d.braun@ucl.ac.uk.

Notes
The authors declare no competing financial interest.

■ ACKNOWLEDGMENTS

■ REFERENCES

(1) Brittain, H. G.; Morris, K. R.; Boerrigter, S. X. M. In *Polymorphism in Pharmaceutical Solids*, 2 ed.; Brittain, H. G., Ed.; Informa Healthcare USA, Inc.: New York, 2009; pp 233−281.
(2) Threlfall, T. L. *Analyst* **1995**, *120*, 2435−2460.
(3) Infantes, L.; Chisholm, J.; Motherwell, S. *CrystEngComm* **2003**, *5*, 480−486.
(4) Stahly, G. P. *Cryst. Growth Des.* **2007**, *7*, 1007−1026.
(5) Griesser, U. J. In *Polymorphism: In the Pharmaceutical Industry*; Hilfiker, R., Ed.; Wiley-VCH: Germany, 2006; pp 211−233.
(6) Braun, D. E. Crystal Polymorphism of Drug Compounds: Statistical Aspects, Analytical Strategies and Case Studies. Ph.D. Thesis, University of Innsbruck, 2008.
(7) European Pharmacopoeia 5.8; Council of Europe European (COE) − European Directorate for the Quality of Medicines (EDQM), 2007.
(8) Brittain, H. G. *Polymorphism in Pharmaceutical Solids*; Informa Healthcare: New York, 2009; Vol. *192*.
(9) Khankari, R. K.; Grant, D. J. W. *Thermochim. Acta* **1995**, *248*, 61−79.
(10) Sun, C.; Grant, D. J. W. *Pharm. Res.* **2004**, *21*, 382−386.
(11) Braun, D. E.; Karamertzanis, P. G.; Arlin, J. B.; Florence, A. J.; Kahlenberg, V.; Tocher, D. A.; Griesser, U. J.; Price, S. L. *Cryst. Growth Des.* **2011**, *11*, 210−220.
(12) Aaltonen, J.; Alleso, M.; Mirza, S.; Koradia, V.; Gordon, K. C.; Rantanen, J. *Eur. J. Pharm. Biopharm.* **2009**, *71*, 23−37.
(13) Cui, Y.; Yao, E. *J. Pharm. Sci.* **2008**, *97*, 2730−2744.
(14) Braun, D. E.; Karamertzanis, P. G.; Price, S. L. *Chem. Commun.* **2011**, *47*, 5443−5445.
(15) Karamertzanis, P. G.; Anandamanoharan, P. R.; Fernandes, P.; Cains, P. W.; Vickers, M.; Tocher, D. A.; Florence, A. J.; Price, S. L. *J. Phys. Chem. B* **2007**, *111*, 5326−5336.
(16) Braun, D. E.; Ardid-Candel, M.; D'Oria, E.; Karamertzanis, P. G.; Arlin, J. B.; Florence, A. J.; Jones, A. G.; Price, S. L. *Cryst. Growth Des.* **2011**, *11*, 5659−5669.
(17) Wallwork, S. C.; Powell, H. M. *Acta Crystallogr.* **1957**, *10*, 48−52.
(18) Maartmann-Moe, K. *Acta Crystallogr.* **1965**, *19*, 155−157.
(19) Wisespongpand, P.; Kuniyoshi, M. *J. Appl. Phycol.* **2003**, *15*, 225−228.
(20) Singh, I. P.; Sidana, J.; Bansal, P.; Foley, W. J. *Expert Opin. Ther. Pat.* **2009**, *19*, 847−866.
(21) Xu, S.; Yang, S. *Huaxue Tongbao* **2007**, *70*, 582−699.

(22) Singh, I. P.; Bharate, S. B. *Nat. Prod. Rep.* **2006**, *23*, 558−591.
(23) Pal, S., I; Bharate, S. B. *Nat. Prod. Rep.* **2006**, *23*, 558−591.
(24) Kim, M.; Kim, S. *Food Chem. Toxicol.* **2010**, *48*, 2925−2933.
(25) Kang, K. A.; Zhang, R.; Chae, S.; Lee, S. J.; Kim, J.; Kim, J.; Jeong, J.; Lee, J.; Shin, T.; Lee, N. H.; Hyun, J. W. *Chem.—Biol. Interact.* **2010**, *185*, 215−226.
(26) Lu, W.; Liu, X.; Wu, B.; Lu, W. Preparation of orally-disintegrating tablets of phloroglucinol as antispasmodic for treating smooth muscle spasm. Chinese Patent CN A 101461788, 20090624.
(27) Bowden, K.; Ross, W. J. *J. Pharm. Pharmacol.* **1965**, *17*, 239−242.
(28) Mandix, K.; Colding, A.; Elming, K.; Sunesen, L.; Shim, I. *Int. J. Quantum Chem.* **1993**, *46*, 159−170.
(29) Groth, P. *Chemische Krystallographie. Teil 4. Aromatische Kohlenstoffverbindungen mit einem Benzolringe*; Engelmann, W.: Leipzig, Germany, 1917; Vol. 4.
(30) Banerjee, K.; Ahmad, R. *Indian J. Phys.* **1938**, *12*, 249−258.
(31) Bose, C. R.; Sen, R. *Indian J. Phys.* **1943**, *17*, 163−165.
(32) Chorgade, S. L. *Proc. Natl. Acad. Sci. India* **1943**, 261.
(33) Singh, S. R.; Singh, G. *J. Cryst. Growth* **1978**, *44*, 581−586.
(34) Saha, B. K.; Nath, N. K.; Ashwini, N. Personal communication, 2009.
(35) Thomas, L. H.; Craig, G. A.; Morrison, C. A.; Reilly, A. M.; Wilson, C. C. *Cryst. Growth Des.* **2011**, *11*, 2045−2049.
(36) Rudyk, R.; Molina, M. A. A.; Yurquina, A.; Gomez, M. I.; Blanco, S. E.; Ferretti, F. H. *J. Mol. Struct.* **2004**, *673*, 231−238.
(37) Dewit, H. G. M.; Bouwstra, J. A.; Blok, J. G.; DeKruif, C. G. *J. Chem. Phys.* **1983**, *78*, 1470−1475.
(38) Mammino, L.; Kabanda, M. M. *J. Mol. Struct.* **2008**, *852*, 36−45.
(39) Allen, F. H. *Acta Crystallogr., Sect. B* **2002**, *58*, 380−388.
(40) Gorbitz, C. H.; Kaboli, M.; Read, M. L.; Vestli, K. *Acta Crystallogr., Sect. E.* **2008**, *o2023*, o2023/1−o2023/7.
(41) Lehto, V. P.; Laine, E. *Pharm. Res.* **2000**, *17*, 701−706.
(42) Kim, Y.-S.; Del Rio, J. R. M.; Rousseau, R. W. *J. Pharm. Sci.* **2005**, *94*, 1941−1948.
(43) Zencirci, N.; Gstrein, E.; Langes, C.; Griesser, U. J. *Thermochim. Acta* **2009**, *485*, 33−42.
(44) Uriano, G.A. National Bureau of Standards Certificate. Standard Reference Material 1655, Potassium Chloride, KCl(cr) for Solution Calorimetry, Washington, DC, 1981.
(45) Burla, M. C.; Caliandro, R.; Camalli, M.; Carrozzini, B.; Cascarano, G. L.; De Caro, L.; Giacovazzo, C.; Polidori, G.; Spagna, R. *J. Appl. Crystallogr.* **2005**, *38*, 381−388.
(46) Sheldrick, G. M. *Acta Crystallogr., Sect. .* **2008**, *64*, 112−122.
(47) Farrugia, L. J. *J. Appl. Crystallogr.* **1999**, *32*, 837−838.
(48) Spoliti, M.; Bencivenni, L.; Quirante, J. J.; Ramondo, F. *J. Mol. Struct.* **1997**, *390*, 139−148.
(49) Frisch, M. J.; Trucks, G. W.; Schlegel, H. B.; Scuseria, G. E.; Robb, M. A.; Cheeseman, J. R.; Montgomery, J.; Vreven, T.; Kudin, K. N.; Burant, J. C.; Millam, J. M.; Iyengar, S. S.; Tomasi, J.; Barone, V.; Mennucci, B.; Cossi, M.; Scalmani, G.; Rega, N.; Petersson, G. A.; Nakatsuji, H.; Hada, M.; Ehara, M.; Toyota, K.; Fukuda, R.; Hasegawa, J.; Ishida, M.; Nakajima, T.; Honda, Y.; Kitao, O.; Nakai, H.; Klene, M.; Li, X.; Knox, J. E.; Hratchian, H. P.; Cross, J. B.; Bakken, V.; Adamo, C.; Jaramillo, J.; Gomperts, R.; Stratmann, R. E.; Yazyev, O.; Austin, A. J.; Cammi, R.; Pomelli, C.; Ochterski, J.; Ayala, P. Y.; Morokuma, K.; Voth, G. A.; Salvador, P.; Dannenberg, J. J.; Zakrzewski, V. G.; Dapprich, S.; Daniels, A. D.; Strain, M. C.; Farkas, O.; Malick, D. K.; Rabuck, A. D.; Raghavachari, K.; Foresman, J. B.; Ortiz, J. V.; Cui, Q.; Baboul, A. G.; Clifford, S.; Cioslowski, J.; Stefanov, B. B.; Liu, G.; Liashenko, A.; Piskorz, P.; Komaromi, I.; Martin, R. L.; Fox, D. J.; Keith, T.; Al Laham, M. A.; Peng, C. Y.; Nanayakkara, A.; Challacombe, M.; Gill, P. M. W.; Johnson, B.; Chen, W.; Wong, M. W.; Gonzalez, C.; Pople, J. A. *Gaussian 03*; Gaussian Inc.: Wallingford, CT, 2004.
(50) Karamertzanis, P. G.; Pantelides, C. C. *J. Comput. Chem.* **2005**, *26*, 304−324.
(51) Coombes, D. S.; Price, S. L.; Willock, D. J.; Leslie, M. *J. Phys. Chem.* **1996**, *100*, 7352−7360.

(52) Breneman, C. M.; Wiberg, K. B. *J. Comput. Chem.* **1990**, *11*, 361−373.

(53) Price, S. L.; Leslie, M.; Welch, G. W. A.; Habgood, M.; Price, L. S.; Karamertzanis, P. G.; Day, G. M. *Phys. Chem. Chem. Phys.* **2010**, *12*, 8478−8490.

(54) Stone, A. J. *J. Chem. Theory Comput.* **2005**, *1*, 1128−1132.

(55) Stone, A. J. *GDMA: A Program for Performing Distributed Multipole Analysis of Wave Functions Calculated Using the Gaussian Program System*, version 1.0; University of Cambridge: Cambridge, U.K., 1999.

(56) Kazantsev, A. V.; Karamertzanis, P. G.; Adjiman, C. S.; Pantelides, C. C. In *Molecular System Engineering*, Adjiman, C. S., Galindo, A., Eds.; WILEY-VCH Verlag GmbH & Co.: Weinheim, Germany, 2010; 1−42.

(57) Cooper, T. G.; Hejczyk, K. E.; Jones, W.; Day, G. M. *J. Chem. Theory Comput.* **2008**, *4*, 1795−1805.

(58) Day, G. M.; Cooper, T. G. *CrystEngComm* **2010**, *12*, 2443−2453.

(59) Cossi, M.; Scalmani, G.; Rega, N.; Barone, V. *J. Chem. Phys.* **2002**, *117*, 43−54.

(60) Spek, A. L. *J. Appl. Crystallogr.* **2003**, *36*, 7−13.

(61) Macrae, C. F.; Edgington, P. R.; McCabe, P.; Pidcock, E.; Shields, G. P.; Taylor, R.; Towler, M.; De Streek, J. *J. Appl. Crystallogr.* **2006**, *39*, 453−457.

(62) Chisholm, J. A.; Motherwell, S. *J. Appl. Crystallogr.* **2005**, *38*, 228−231.

(63) Kharchenko, E. V.; Skorobogat'ko, E. P.; Nagornyi, P. G.; Turov, A. V. *Ukr. Khim. Zh.* **1986**, *52*, 612−614.

(64) Braun, D. E.; Gelbrich, T.; Kahlenberg, V.; Tessadri, R.; Wieser, J.; Griesser, U. J. *Cryst. Growth Des.* **2009**, *9*, 1054−1065.

(65) De Wit, H. G. M.; Bouwstra, J. A.; Blok, J. G.; De Kruif, C. G. *J. Chem. Phys.* **1983**, *78*, 1470−1475.

(66) Li, Z. J.; Ojala, W. H.; Grant, D. J. W. *J. Pharm. Sci.* **2001**, *90*, 1523−1539.

(67) Bond, A. D.; Boese, R.; Desiraju, G. R. *Angew. Chem., Int. Ed.* **2007**, *46*, 618−622.

(68) Chan, E. J.; Welberry, T. R.; Heerdegen, A. P.; Goossens, D. J. *Acta Crystallogr., Sect. B: Struct. Sci.* **2010**, *B66*, 696−707.

(69) O'Neal, M. J. *The Merck Index: An Encyclopedia of Chemicals, Drugs, and Biologicals*, 14th ed.; Merck & Co., Inc.: Whitehouse Station, NJ, 2006; entry 7328.

(70) *Reaxys*, version 1.0.9619; Elsevier Properties SA: Frankfurt, Germany, 2011; Reaxys RN 1341907 (accessed Nov 9.2011).

(71) *Scifinder*, v. 2007; Chemical Abstract Services: Columbus, OH, 2007; RN 108-76-3 (accessed Nov 9.2011).

(72) Riddick, J. A.; Bunger, W. B.; Sakano, T. K. *Techniques of Chemistry: Organic Solvents: Physical Properties*, 4th ed; Wiley-Interscience: New York, 1986.

(73) The heat capacity term (difference between the heat capacities of water in vapor and liquid states) was ignored, as we used the heat of vaporization of water at the dehdyration temperature.

(74) Kamb, B.; Hamilton, W. C.; LaPlaca, S. J.; Prakash, A. *J. Chem. Phys.* **1971**, *55*, 1934−1945.

(75) Jorgensen, J. D.; Beyerlein, R. A.; Watanabe, N.; Worlton, T. G. *J. Chem. Phys.* **1984**, *81*, 3211−3214.

(76) Salzmann, C. G.; Radaelli, P. G.; Mayer, E.; Finney, J. L. *Phys. Rev. Lett.* **2009**, *103*, 105701−1−105701/4.

(77) Leadbetter, A. J.; Ward, R. C.; Clark, J. W.; Tucker, P. A.; Matsuo, T.; Suga, H. *J. Chem. Phys.* **1985**, *82*, 424−428.

(78) La Placa, S. J.; Hamilton, W. C.; Kamb, B.; Prakash, A. *J. Chem. Phys.* **1973**, *58*, 567−580.

(79) Salzmann, C. G.; Radaelli, P. G.; Hallbrucker, A.; Mayer, E.; Finney, J. L. *Science* **2006**, *311*, 1758−1761.

(80) Jackson, S. M.; Nield, V. M.; Whitworth, R. W.; Oguro, M.; Wilson, C. C. *J. Phys. Chem. B* **1997**, *101*, 6142−6145.

(81) Khankari, R. K.; Law, D.; Grant, D. J. W. *Int. J. Pharm.* **1992**, *82*, 117−127.

(82) Price, S. L. In *Polymorphism in Pharmaceutical Solids*, 2nd ed.; Brittain, H. G., Ed.; Informa Healthcare USA, Inc.: New York, 2009; pp 52−75.

(83) Tremayne, M.; Grice, L.; Pyatt, J. C.; Seaton, C. C.; Kariuki, B. M.; Tsui, H. H. Y.; Price, S. L.; Cherryman, J. C. *J. Am. Chem. Soc.* **2004**, *126*, 7071−7081.

(84) Copley, R. C. B.; Barnett, S. A.; Karamertzanis, P. G.; Harris, K. D. M.; Kariuki, B. M.; Xu, M. C.; Nickels, E. A.; Lancaster, R. W.; Price, S. L. *Cryst. Growth Des.* **2008**, *8*, 3474−3481.

(85) Habgood, M. *Cryst. Growth Des.* **2011**, *11*, 3600−3608.